JGR Space Physics

RESEARCH ARTICLE
10.1029/2019JA026728

Key Points:
- Global MHD model with kinetic test particles shows comparable solar wind entry from KH vortices and cusp reconnection under northward IMF
- Solar wind entry exhibits intrinsic dawn-dusk asymmetry due to the preferential energization and dawnward deflection of cusp-entering ions
- Combined flank- and cusp-entering solar wind ions recreates observed two-component (hot and cold) dusk and broad-peaked dawn population

Supporting Information:
- Supporting Information S1
- Figure S1
- Figure S2
- Movie S1

Correspondence to:
K. A. Sorathia,
kareem.sorathia@gmail.com

Citation:
Sorathia, K., Merkin, V. G., Ukhorskiy, A. Y., Allen, R. C., Nykyri, K., & Wing, S. (2019). Solar wind ion entry into the magnetosphere during northward IMF. *Journal of Geophysical Research: Space Physics*, *124*, 5461–5481. https://doi.org/10.1029/2019JA026728

Received 19 MAR 2019
Accepted 29 MAY 2019
Accepted article online 6 JUN 2019
Published online 22 JUL 2019

Solar Wind Ion Entry Into the Magnetosphere During Northward IMF

K. A. Sorathia[1], V. G. Merkin[1], A. Y. Ukhorskiy[1], R. C. Allen[1], K. Nykyri[2], and S. Wing[1]

[1]The Johns Hopkins University Applied Physics Laboratory, Laurel, MD, USA, [2]Center for Space and Atmospheric Research, Embry-Riddle Aeronautical University, Daytona Beach, FL, USA

Abstract Extended periods of northward interplanetary magnetic field (IMF) lead to the formation of a cold, dense plasma sheet due to the entry of solar wind plasma into the magnetosphere. Identifying the paths that the solar wind takes to enter the magnetosphere, and their relative importance has remained elusive. Any theoretical model of entry must satisfy observational constraints, such as the overall entry rate and the dawn-dusk asymmetry observed in the cold, dense plasma sheet. We model, using a combination of global magnetohydrodynamic and test particle simulations, solar wind ion entry into the magnetosphere during northward IMF and compare entry facilitated by the Kelvin-Helmholtz instability to cusp reconnection. For Kelvin-Helmholtz entry we reproduce transport rates inferred from observation and kinetic modeling and find that intravortex reconnection creates buoyant flux tubes, which provides, through interchange instability, a mechanism of filling the central plasma sheet with cold magnetosheath plasma. For cusp entry we show that an intrinsic dawn-dusk asymmetry is created during entry that is the result of alignment of the westward ion drift with the dawnward electric field typically observed during northward IMF. We show that both entry mechanisms provide comparable mass but affect entering plasma differently. The flank-entering plasma is cold and dawn-dusk symmetric, whereas the cusp-entering plasma is accelerated and preferentially deflected toward dawn. The combined effect of these entry mechanisms results in a plasma sheet population that exhibits dawn-dusk asymmetry in the manner that is seen in nature: a two-component (hot and cold) dusk flank and hotter, broadly peaked dawn population.

1. Introduction

The terrestrial plasma sheet separates the northern and southern lobes of the Earth's magnetotail and serves as a repository for the majority of the plasma mass in the magnetotail. Atmospheric precipitation and tailward flow result in the continual loss of plasma, estimated to be 10^{25}–10^{26} particles per second during quiet times and up to 100 times more during periods of high geomagnetic activity (Wing et al., 2014). These losses are balanced by the inflow of plasma, either from the solar wind or ionosphere, into the plasma sheet. Wing et al. (2014) recently provided a comprehensive review of the state of understanding of mass regulation within the plasma sheet. It is now known (Wing et al., 2014, and references therein) that the solar wind, primarily during periods of northward interplanetary magnetic field (IMF), is the primary source of plasma sheet mass. Periods of northward IMF lead to the formation of a cold, dense plasma sheet (CDPS). Important questions remain, however, regarding the path, or paths, that solar wind plasma takes to enter the terrestrial magnetosphere and how entering plasma evolves during its journey.

Wing et al. (2014) discuss four, not mutually exclusive, entry mechanisms during northward IMF: double cusp reconnection, Kelvin-Helmholtz (KH) waves on the magnetopause boundary, kinetic Alfven waves (KAWs), and impulsive penetration due to magnetosheath irregularities. The relative importance and characteristics of these entry mechanisms are currently unsettled, but an important discriminator is the observed dawn-dusk asymmetry (Wing et al., 2005) of the CDPS in density and temperature. The density of the dawnside plasma sheet is generally observed to be higher than that of the duskside. It is also often observed that the duskside plasma sheet plasma is composed of two thermally disjoint populations, a hot and cold component, whereas the dawnside plasma is observed to have one component with a broad peak in energy spectrum (Hasegawa et al., 2003). The two components themselves are observed to exhibit temperature anisotropies that vary based on the location within the magnetosphere (Nishino et al., 2007). Modeling approaches to study entry have, by necessity, advanced on multiple fronts as there is no single framework to simulate the dynamic range of scales that these mechanisms act over: global magnetospheric scales, $\geq 10R_E$, over which double cusp reconnection and the full life cycle of KH vortices occur; mesoscale, $\sim 1\ R_E$, over which the plasma irregularities that induce impulsive penetration occur and the scale at which turbulent transport and intravortex magnetic field topology changes manifest in KH waves; and kinetic scales, below the ion gyroradius and inertial lengthscales, at which magnetic reconnection truly occurs and over which nonideal effects such as nonzero $E_{\|}$ typically manifest (Hesse et al., 1999).

In this work our focus will be on the first two mechanisms, double cusp reconnection and KH waves. Specifically, using global magnetohydrodynamic (MHD) and test particles simulation, we study the relative importance of these two mechanisms and how together they can create similar dawn-dusk asymmetry to what is observed. Kinetic effects, such as KAW or kinetic magnetosonic waves (Moore et al., 2016), are outside the domain of applicability of our ideal MHD model. Our choice of simulation is by construction idealized in its symmetry as we wish to isolate plasma sheet dawn-dusk asymmetry *created* by entry mechanisms, that is, intrinsic, from asymmetry that is inherited from or a reflection of other asymmetries, that is, extrinsic effects. Consequently, we do not expect impulsive entry to play an important role in our simulations.

Previous modeling work on these two entry mechanisms, double cusp reconnection and KH waves, has been conducted separately: with global ideal MHD simulations used to study the former and spatially localized more sophisticated models (resistive, hybrid, and kinetic) used to study the latter. Global MHD has long been capable of modeling the transfer of plasma from the magnetosheath into the plasma sheet (Fedder & Lyon, 1995; Raeder et al., 1995). More recent work has focused more directly on the study of solar wind entry. Li et al. (2008) conducted an extensive parameter study exploring the effect of varying solar wind and geomagnetic parameters on the cusp entry rate using global MHD (Raeder et al., 1998) and fluid element tracing. Peroomian and El Alaoui (2008) and Peroomian et al. (2011) used a global MHD and test particle approach to study ion transport to the plasma sheet during chosen geomagnetic storm events. Welling and Ridley (2010) used multispecies MHD, separating ionospheric from solar originating fluid, to study mass entry during both southward and northward IMF. These global studies of solar wind entry largely focused on cusp reconnection and either did not find or did not remark upon appreciable KH entry. This is unsurprising as it is only more recently, and at great computational expense, that global MHD simulations of the magnetosphere have been able to produce realistic KH dynamics (Guo et al., 2010; Merkin et al., 2013).

Modeling KH transport has largely been the focus of more specialized simulations, exploiting reduced dimensionality, simplified geometry, and utilizing more sophisticated physical models. Johnson et al. (2014) recently provided a comprehensive review of the study of KH in planetary magnetospheres. Miura (1984, 1987) first studied momentum transport across the magnetopause due to Kelvin-Helmholtz instability (KHI). As an ideal instability, KHI was not expected to produce plasma transport. Otto and Fairfield (2000) were the first to notice, using local resistive MHD, that reconnection in KH vortices can detach large, high-density islands of magnetosheath origin. Subsequent two-dimensional MHD modeling was used to quantitatively analyze mass transport due to KHI (e.g., Nykyri & Otto, 2001; Otto & Nykyri, 2003) and more recently in 3-D (e.g., Ma et al., 2017). Local MHD has also been used to study the modulation of KH due to extrinsic drivers (e.g., Adamson et al., 2016; Nykyri, 2013; Nykyri et al., 2017). Transport via KH has also been studied using models that incorporate kinetic physics: hybrid (e.g., Cowee et al., 2009, 2010) and kinetic (e.g., Nakamura et al., 2013, 2017). Throughout these studies, mass transport mediated by KH waves has often been quantified using an approximate diffusion coefficient, albeit not necessarily calculated in precisely the same manner. Typically, it is estimated between 10^9 and 10^{10} m^2/s in agreement with early estimates of diffusive mass transport in the low-latitude boundary layer (LLBL) by Sonnerup (1980). However, Cowee et al. (2009) make the important point that KH transport is not diffusive in a classical sense and that enhanced transport can occur due to coherent vortices. A primary goal of this work is to take a first step toward bridging the gap between global and local models by demonstrating that we can reproduce appropriate KH transport rates within a global magnetospheric simulation and consequently contrast cusp and KH entry quantitatively.

The other primary goal of this work is to address the observed dawn-dusk asymmetry by separating *intrinsic* from *extrinsic* sources of dawn-dusk asymmetry in the plasma sheet population. A variety of factors related to the state of the solar wind or of the magnetosphere have been discussed as potential contributors to the observed asymmetry: solar wind speed (Wang et al., 2007), heavy ion distribution (Johnson et al., 2014), ionospheric conductance (Zhang et al., 2012), and solar wind IMF orientation (Adamson et al., 2016). We show here, using an idealized global magnetosphere, that ion entry through the geomagnetic cusp creates an intrinsic dawn-dusk asymmetry. Simulated ions that enter through the cusp are accelerated in the cusp diamagnetic cavity (DMC; Niehof et al., 2010; Nykyri et al., 2012) and preferentially deflected toward dawn, whereas simulated ions that enter through the magnetospheric flanks are cold and dawn-dusk *symmetric*. The combined ion population then consists of the dawn population (cold flank-entering particles and a broad range of accelerated cusp-entering particles) and the dusk population (cold flank-entering particles and cusp-entering particles energetic enough to cross the central plasma sheet from dawn to dusk). These results do not address extrinsic sources of asymmetry. In a more realistic magnetosphere these extrinsic effects may play an important role in addition to the intrinsic asymmetry we demonstrate here.

We address the issues described above using a combination of global MHD and test particles, detailed in section 2. An ensemble of test particles matching the solar wind parameters is injected upwind of the bowshock into a global MHD simulation of the magnetosphere during northward IMF. Capturing the trajectories of the test particles that enter the magnetosphere allows us to distinguish particle dynamics associated with different entry mechanisms (double cusp reconnection or KHI). Using this framework, we will show that both double cusp reconnection and KH waves facilitate a comparable amount of mass transport into the magnetosphere (section 3.1). We show that the properties of the two disparate populations, flank- and cusp-entering ions, lead to dawn-dusk asymmetry as observed (section 3.2). We then provide separate analyses of the flank- and cusp-entering populations. In section 3.3 we estimate the efficacy of transport via KH waves and demonstrate a correlation between plasma sheet transport and global entropy distribution (section 3.3.2). Section 3.4 focuses on the energization of cusp-entering particles and their dawnward bias. Finally, section 4 includes a summary of our results and a discussion of their context within the larger body of work on mass transport within the plasma sheet.

2. Methodology

Our methodology builds on the approach described in detail in Appendix 1 of Sorathia et al. (2018). Combining global MHD and test particle simulations allows us to simultaneously capture both global and mesoscale dynamics, for example, Kelvin-Helmholtz vortices, that can facilitate solar wind entry and drift physics beyond the $\vec{E} \times \vec{B}$ drift of the MHD flow, which we find leads to dawn-dusk asymmetry and particle energization during the entry process. In the remainder of this section we describe the salient details of our simulation pipeline, which consists of global electromagnetic fields that are generated using the Lyon-Fedder-Mobarry (LFM) MHD code (Lyon et al., 2004) to simulate the Earth's magnetosphere during northward IMF, an ensemble of test particles used to model a thick “wall” of solar wind created upstream of the Earth's bow shock using our test particle code CHIMP (Sorathia et al., 2018), and the magnetic field topology diagnostics we use to identify particle entry.

The global MHD simulation we utilize is almost identical to that presented in Merkin et al. (2013), differing only in that we use a slightly lower solar wind velocity (400 km/s instead of 600 km/s). The LFM model simulates the global magnetosphere using a distorted spherical grid contained within a cylindrical domain with symmetry axis aligned with the solar magnetic (SM) X axis. The outer boundaries of the cylinder are at $X_{\mathrm{SM}} = 30R_E$ and $X_{\mathrm{SM}} = -330R_E$ and its cross-sectional radius is $125R_E$. We use the highest-resolution LFM grid (“OCT”) of size $212 \times 256 \times 192$ cells in the radial, polar, and azimuthal directions (with respect to the X axis). The highly distorted nature of the simulation grid allows us to concentrate cells in regions of interest, for example, the magnetopause and plasma sheet, while smoothly transitioning to coarser regions. Of importance here is that the radial cell size at the flank magnetopause is $\Delta R \approx 0.1R_E$, which ensures that we can resolve the boundary dynamics (see also Figure 1 of Sorathia et al., 2017). The magnetosphere is preconditioned with periods of alternating southward and northward IMF (described previously in Merkin et al., 2013; Wiltberger et al., 2015) after which the solar wind is held fixed with constant density (5 cm^{-3}), velocity ($V_x = -400$ km/s and $V_y = V_z = 0$), and IMF ($B_z = +5$ nT and $B_x = B_y = 0$). The inner boundary condition of the simulation, imposed on a spherical surface of radius $2R_E$ centered on Earth, is a constant conductance ionosphere with $\Sigma_P = 10S$ and $\Sigma_H = 0S$ and no dipole tilt was applied. A detailed description of the ionospheric solver and its coupling to the magnetosphere is provided in Merkin and Lyon (2010). This simulation is idealized, as by construction we seek to maximize the symmetry of the magnetospheric state to isolate dawn-dusk asymmetries that are intrinsic to the entry process.

The entry of solar wind plasma into the magnetosphere is tracked by creating a population of test particles injected over time upstream of the bowshock. For a period of 1 hr, beginning at what we define to be $T = 0$, we continuously inject proton test particles into a cylindrical polar domain $(R, z) \in [22.0, 22.5] \times [-25, 25]$ and $\pm 45°$ of magnetic noon. Equivalently, we create a wall of solar wind using test particles that is approximately 200 R_E deep, 30 R_E wide, and 50 R_E high. The height and width of this region were chosen after verifying that a larger injection region does not contribute to further magnetospheric entry. The proton test particles are initialized with a random pitch angle relative to the IMF and an energy of 10 eV in the frame of reference moving with the solar wind flow. In total, we inject 50 million test particles into the simulation domain. The period of injection begins 1 hr after the final northward turn to avoid the potential effects of remnant reconnection. After the period of active injection, $T = [0, 1]$ hr, test particles that remain within the LFM simulation domain are evolved until $T = 3$ hr.

Proton test particles are evolved by solving the Lorentz equations of motion in the ambient MHD-generated fields using the approach described in Sorathia et al. (2018) with several recently implemented improvements. While the previous iteration of the CHIMP code used an intermediate Cartesian grid to store electromagnetic field information, now all electromagnetic field interpolation, trajectory calculations, and field line tracing are done on the native LFM grid. We have also replaced the use of multilinear spatial interpolation with triangular-shaped cloud (Hockney & Eastwood, 1981; Lehe et al., 2009), a higher-order interpolant with superior regularity, although its use for curvilinear meshes requires the further step of numerically inverting the mapping between physical and logical coordinates.

Our electromagnetic fields are calculated using an ideal MHD simulation and for test particle interpolation we use the convective electric field, $\vec{E} = -\vec{V} \times \vec{B}$, using the cell-centered velocity and magnetic field. Ideal MHD implies the orthogonality of the electric and magnetic fields; that is, $\vec{E}_{\parallel} = 0$, which will be satisfied at the cell centers from which we interpolate. However, when interpolating individual electromagnetic field components the interpolated fields will not, in general, satisfy $\vec{E} \cdot \vec{B} = 0$. This will introduce a parallel electric field due to interpolation error, and while this field will be small, we find that the entry process is sensitive to the existence of nonzero $\vec{E}_{\parallel}$. As described in Sorathia et al. (2018, equation (A12)), we correct our interpolated electric field by removing any parallel component. Comparing test particle simulations with and without this electric field correction, we find that even a small $\vec{E}_{\parallel}$, whose origin is interpolation error, can significantly increase the number of solar wind test particles that enter the magnetosphere. While this is a numerical effect, it does suggest that solar wind entry is sensitive to parallel electric fields, which may be physical in reality, such as KAWs (Wing et al., 2014).

2.1. Diagnostics

Our goal in this work is to study the entry of solar wind plasma into the magnetosphere; in particular, we wish to identify *where* particles enter the magnetosphere in order to quantify the relative importance of different entry mechanisms. To this end, we proceed in a manner similar to Sorathia et al. (2017) and periodically trace the local magnetic field at the position of each test particle and identify the local magnetic topology. We categorize each traced field line as closed, open, or IMF based on whether both, one, or neither end of the field line connects to the inner radial boundary of the simulation domain at $R = 2R_E$. This field line tracing is used to identify where test particles transition from the solar wind, or IMF, magnetic field to terrestrial, defined as open or closed, magnetic field lines. In other words, we identify the point in space and time when a test particle is no longer attached to the IMF.

The cadence at which we trace field lines is informed by the characteristic time scales for solar wind particles after they enter the magnetosphere. Using a typical particle energy of $K \approx 1$ keV and $L = 10$, for an approximate magnetopause location, the bounce and drift time scales (assuming $L = 10$ and a dipole magnetic field) will be several minutes and days, respectively. Using a field line tracing cadence of $\Delta t = 10$ s, significantly smaller than either time scale, we can ensure that test particles will not move significantly in longitude or latitude during a field line tracing interval.

From the total 50 million solar wind test particles we simulate, we identify test particles as having entered the magnetosphere based on the following criteria: a test particle that transitions from the IMF to closed field lines and remains on closed field lines for a continuous period of time longer than 30 min. The number of test particles identified as entering the magnetosphere is generally insensitive to this choice of time interval as long as the period of time on which test particles must remain on closed field lines is greater than several minutes. Using this definition, we find approximately 50,000 test particles that enter the magnetosphere.

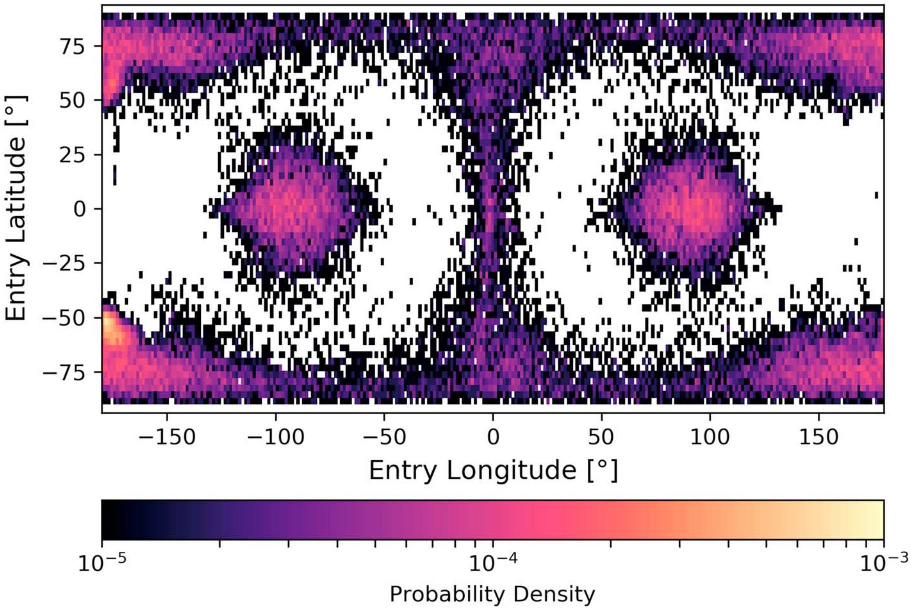

Figure 1. Spherical geometry of solar wind entry. Statistical distribution of the location of test particles, in longitude and latitude as defined by equations (1) and (2), at time of first contact with terrestrial, either open or closed, magnetic field lines.

For each test particle we identify in this manner, we can quantify its point of entry as the point (in SM coordinates) (X_E, Y_E, Z_E) and time (T_E) at which the particle first makes contact with terrestrial magnetic field lines, that is, transitioning from IMF to open or closed field lines. From this we can define the entry longitude, or magnetic local time (MLT), as

$$\phi_E = \arctan(Y_E/X_E), \tag{1}$$

and entry latitude as

$$\lambda_E = \arcsin(Z_E/r_E), \tag{2}$$

where r_E is the radial distance of the entry point. Using this definition of longitude, magnetic noon, dusk, midnight, and dawn correspond to $\phi_E = 0°, 90°, \pm 180°, -90°$, respectively and $\lambda_E = 0°$ is the SM equator.

3. Results

3.1. Overview

Prior to undertaking a more detailed analysis, we begin by calculating an estimated entry rate. While this entails weighting the test particles, that is, converting the test particles to macroparticles, this can be done in a much simpler way than the one described in Appendix 2 of Sorathia et al. (2018). The solar wind flow is uniform in space and time in the injection region, and the solar wind is sufficiently cold that we can uniformly weight the test particles based on the solar wind density, velocity, and the surface area and duration of injection. Averaging over the period of injection gives an estimate of the entry rate as 1.28×10^{27} particles per second. This is well in line with previous estimates from simulation (Li et al., 2008) and observation (Wing et al., 2006).

Moving beyond aggregate entry, the value of simulations like this is that we can more quantitatively study the geometry of solar wind entry, that is, where solar wind plasma transitions to terrestrial field lines, and its characteristic temporal variability. Note that although we use the term "entry" as in previous literature on this topic, this terminology can be somewhat misleading. Solar wind plasma can transition from IMF to closed field lines due to topology changes, for example, cusp reconnection, that occur far away from the location of the particle.

Figure 1 shows the collected statistics of where solar wind test particles enter the magnetosphere. These statistics illustrate that solar wind test particles enter the magnetosphere in a small number of localized

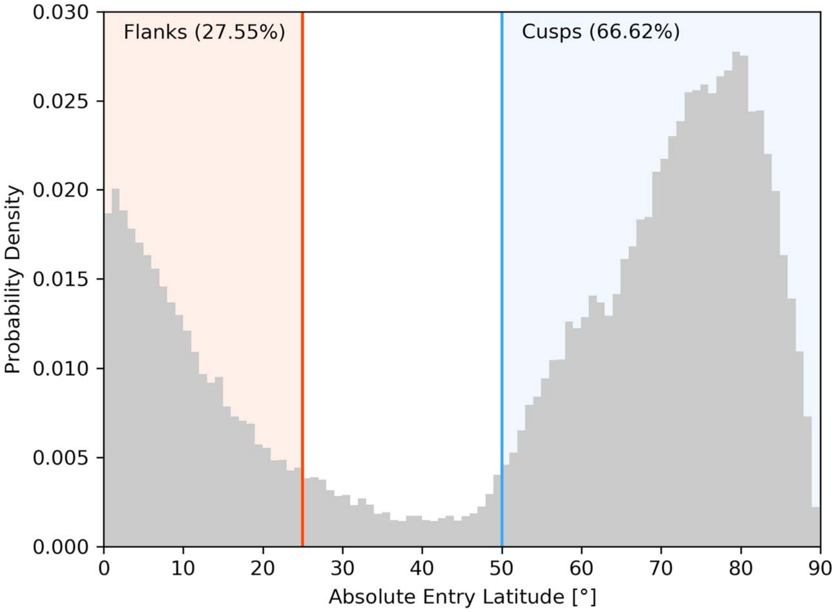

Figure 2. Separation of flank and cusp entry. Statistical distribution of the magnitude of latitude, in solar magnetic coordinates, at time of first contact with terrestrial, either open or closed, magnetic field lines. The relative number of low-latitude (red) and high-latitude (blue) entry particles, denoted flank and cusp, are separately calculated.

regions with approximate dawn-dusk and north-south symmetry. At low latitude, $|\lambda_E| \leq 25°$, entry occurs within two isolated regions spanning approximately 4 hr in MLT and centered on dawn and dusk. At high latitude, $|\lambda_E| \geq 50°$, entry occurs within two isolated regions in the Northern and Southern Hemispheres spanning approximately 6 hr in MLT and centered at midnight. These regions account for the vast majority of total entry, approximately 95%, as shown in Figure 2, the statistical distribution of $|\lambda_E|$.

The location of these regions immediately suggest an interpretation: low-latitude entry that is facilitated by Kelvin-Helmholtz (KH) vortices that are most intense downtail of the subsolar point and high-latitude entry that is facilitated by double cusp reconnection that occurs slightly antisunward of Earth. The clear spatial separation of these entry points allows us to categorize the entering test particles into two populations: flank entry, $|\lambda_E| \leq 25°$, either through the dawn or dusk flanks, and cusp entry, $|\lambda_E| \geq 50°$, either through the northern or southern cusps. Figure 2 shows that cusp entry is responsible for the majority of the total entering population but that flank entry is comparable. In the remainder of our analysis we will separate these two populations based on their point of entry into the magnetosphere, *flank* or *cusp*, to explore the effects these disparate entry mechanisms have on the spatial, temporal, and thermodynamic characteristics of the mass inside the magnetosphere.

Figure 3 provides an overview of the results of our simulation, showing the state of the flank- and cusp-entering test particles overlaid on the global MHD magnetic fields at several representative snapshots. The visualization uses equatorial data for clarity, but both the global MHD and test particle simulations are done in a fully 3-D manner. Figure 3 shows the simulation state at several snapshots in time, starting at midway through the period of active test particle injection ($T = 30$ min) and subsequently at 60-min intervals. The residual magnetic field, that is, the nondipolar component of the vertical magnetic field, is shown at each snapshot in addition to solid color contours representing the boundary between closed and open magnetic field lines (green) and between open and IMF magnetic field lines (blue). Solar wind test particles that have recently crossed the equator, defined as within 5 min of the chosen time, are marked at the location of their most recent crossing of the equatorial plane ($Z_{\mathrm{SM}} = 0$). Displayed test particles are colored by their energy using different color palettes for cusp-entering and flank-entering test particles, classified by the latitude of their point of entry as shown in Figure 2. The surface area of the test particle markers is scaled to increase with energy.

Many of the effects we will analyze in greater detail in the sections below are qualitatively illustrated in Figure 3 and are worth pointing out here. Flank-entering test particles are characterized as a dawn-dusk

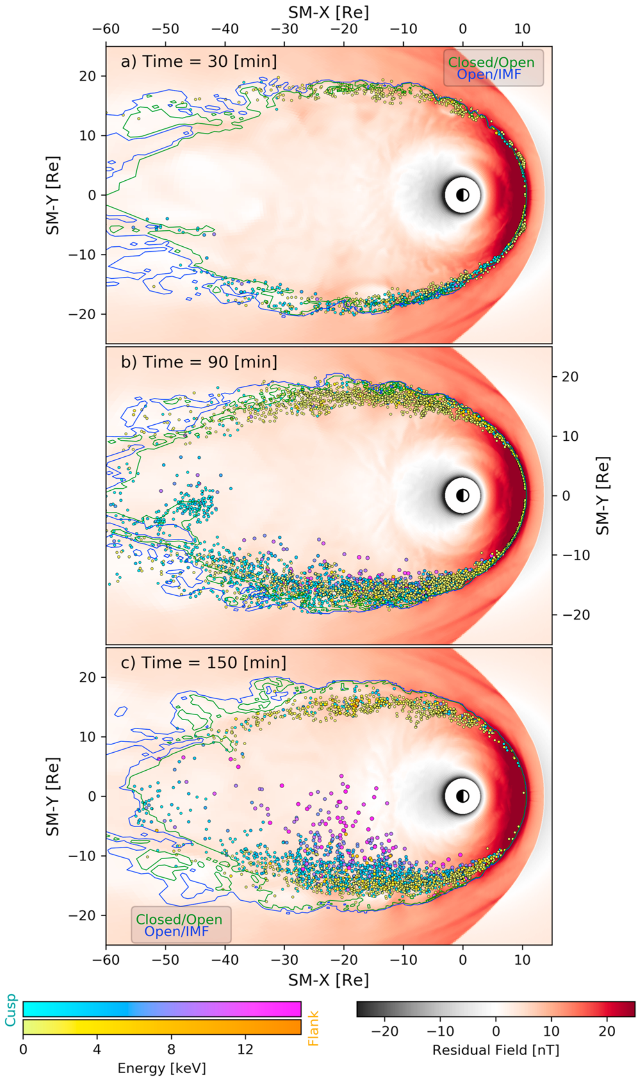

Figure 3. Simulation at a glance. Several chosen snapshots of simulation state shown in the equatorial plane. Background color (bottom right color bar) denotes residual, that is, nondipolar, vertical magnetic field. Test particles that have entered the magnetosphere, defined as being currently on closed field lines, and have recently crossed the equator, defined as within 5 min of the chosen time, are marked at the location of their most recent crossing of the equatorial plane and colored by their energy using separate color maps (bottom left) based on whether their point of entry was through the flank or cusp. Solid contours mark the boundary between interplanetary magnetic field-open (blue) and open-closed (green) field lines.

symmetric, cold population that slowly and symmetrically moves inward toward the central plasma sheet over time. The KH vortices seen in our simulation exhibit the filamentary structure discussed by Nykyri and Otto (2001; e.g., Figure 1 therein) as a signature of mass transport facilitated by KH-driven reconnection. Specifically, we find within these vortices disconnected regions of closed field topology, for example, $(X_{\mathrm{XM}}, Y_{\mathrm{SM}}) \approx (-30, 15)$ in Figure 3c. This suggests the importance of reconnection for flank entry, a point we return to in section 3.3.2.

Whereas the flank-entering particles are symmetric and cold, the cusp-entering particles are the opposite. These particles exhibit a strong bias toward equatorial crossings at the dawn flank and exhibit appreciably higher energies. Over time many of these cusp-entering particles are swept downtail and eventually evacuated but more energetic particles move toward the central plasma sheet much more rapidly than their flank-entering counterparts. Figure 3c shows cusp-entering particles in the central plasma sheet within 2.5 hr of the initial injection period. This is consistent with observational findings (Borovsky et al., 1998) that there is an approximately 2-hr correlation time scale with plasma sheet density and solar wind conditions.

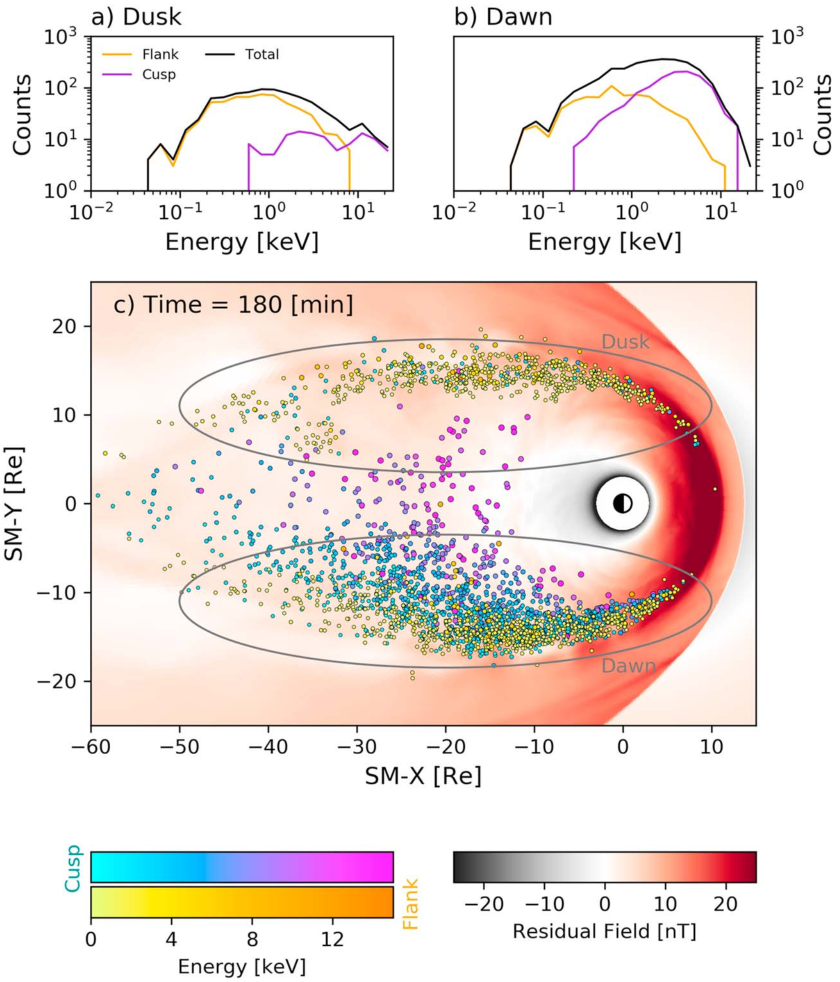

Figure 4. The top panels show energy distribution of test particles at the end of the simulation. Test particles are separated based on their location, either dusk (top left) or dawn (top right) with the geometric boundary of those regions marked on the bottom panel. The bottom panel shows the end state of the simulation in the same manner as Figure 3.

Plasma entry, facilitated by magnetic reconnection and boundary instabilities, is an intrinsically dynamic, three-dimensional process and as such is not easily distilled into a handful of 2-D still images. Within the supporting information we provide several items to better capture the dynamical nature of these processes. Movie S1 contains an animation of the time slices shown in Figure 3. Figures S1 and S2 show a handful of example test particle trajectories for both flank-entering (Figure S1) and cusp-entering (Figure S2) particles projected onto X-Y, X-Z, and Y-Z planes. Finally, we include in Data Set S1 a collection of test particle trajectories, selected from the test particles that enter and remain within the magnetosphere.

3.2. Asymmetry and Variability in Magnetospheric Entry

In the previous section we observed that flank-entering particles can be characterized as cold and dawn-dusk symmetric, whereas cusp-entering particles are more energetic and strongly biased toward dawn. It is a clear benefit of simulations that we can so easily disentangle the two populations, and we take advantage of this fact by analyzing each entry mechanism separately in sections 3.3 and 3.4. However, to connect our model results to the observed formation of the CDPS during northward IMF, it is useful to consider the net effect of the aggregate population on the mass and thermodynamic properties of the plasma sheet. To aid in this, we show in Figure 4c the entering test particles at the end of the simulation in a similar manner to Figure 3 and show the energy distribution of test particles on the dusk (Figure 4a) and dawn (Figure 4b) magnetospheric flanks. Table 1 displays the average energy per population in each region, defined by the marked ellipses shown in Figure 4, at the end of the simulation.

Table 1
Average Energy per Population at End of Simulation

Region \ Energy (keV)	Flank	Cusp	Combined
Dawn	1.108	3.828	2.490
Dusk	1.156	5.497	1.960

Observational studies of magnetospheric entry during northward IMF have shown dawn-dusk asymmetry in the distribution of entering mass and energy density. Higher mass is observed on the dawnside magnetosphere than on the duskside (Hasegawa et al., 2003; Wing et al., 2005) as are higher temperatures (Allen et al., 2017; Wing et al., 2005). It has also been found that during northward IMF (Fujimoto et al., 1998), the duskside ion population is characterized by the combination of a hot and cold component, whereas the dawnside ion population is characterized by a single, broadly peaked component. These two components, hot and cold, when clearly separable typically have temperatures $T_H > 3$ keV and $T_C < 3$ keV, respectively (Hasegawa et al., 2004).

Despite being idealized and symmetric, Figure 4 shows that the simulation matches well with the observed dawn-dusk phenomenology. Mass and energy asymmetry is attributable to the cusp-entering particles, while the flank-entering particles provide a symmetric background. The combined population on the dawn flank is heavier and on average hotter than the dusk flank (Table 1). Cusp-entering particles display a smoothly varying range of energies on the dawn flank; however, the transit from dawn to dusk exhibits an energy filtering effect. More energetic cusp-entering particles are able to transit across the central plasma sheet from dawn to dusk due to their stronger gradient and curvature drifts, whereas less energetic cusp-entering particles are more likely to be swept tailward. Somewhat counterintuitively, this results in a *hotter* cusp-entering population at dusk than dawn (Table 1), with average energies being 5.5 keV (dusk) and 3.8 keV (dawn). As only the more energetic cusp-entering particles contribute to the dusk population, this energy filter effect creates a two-component behavior at the dusk flank: The cusp-entering population is characterized by 5.5 keV, whereas the flank-entering population is only 1.15 keV. We note that this is an intrinsic source of dawn-dusk asymmetry in that it occurs even in an idealized magnetosphere. We discuss the origin of this asymmetry, namely, the energization and dawnward deflection of cusp-entering particles, in more detail in section 3.4.

While our simulation does compare favorably with the qualitative asymmetry observed in nature, it is not our expectation that this idealized model should quantitatively reproduce any specific event. For instance, Nishino et al. (2007), using a selection of several Geotail events, find the emergence of two-component protons near midnight typically within 3 after the arrival of strongly northward IMF. As seen in Figure 4, relatively few flank-entering particles are within $\pm 10 R_E$ of midnight after 3 hr of test particle integration.

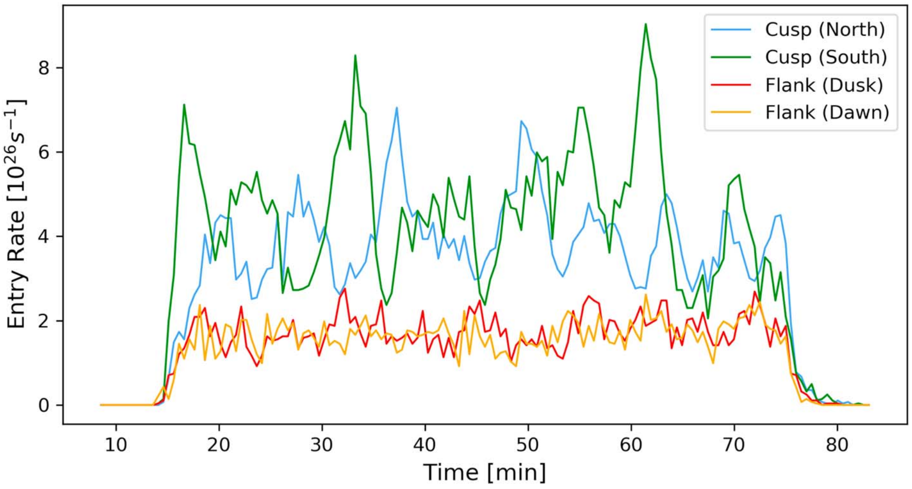

Figure 5. Instantaneous rate of entry of solar wind particles into the magnetosphere as a function of time and separated by entry location.

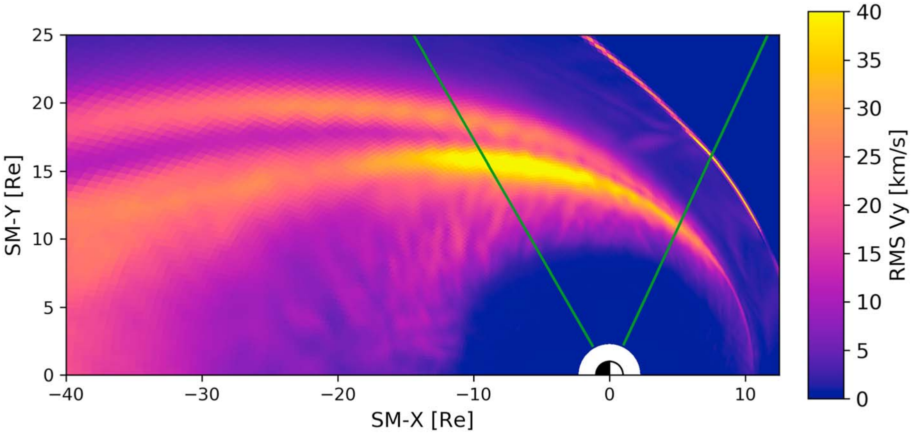

Figure 6. Comparison of root-mean-square (RMS) dawn-dusk velocity (right color bar) and the magnetic local time region of peak flank entry, between the solid green lines (cf. Figure 1).

Further work utilizing more realistic solar wind parameters and ionospheric conductance models is necessary to make quantitative comparisons to specific instances of CDPS formation. We also note that we have purposefully delayed the injection of test particles for 1 hr after the beginning of northward IMF. This is to avoid the effects of remnant nightside reconnection, which we have found to affect the transport of test particles throughout the nightside magnetosphere. The interplay between dayside IMF and remnant nightside behavior can potentially play an important role in the time scale for two-component protons to manifest.

In section 3.1 we discussed the aggregate entry rate, averaged over time, and all entering particles. However, as shown by Figure 5, the instantaneous rate of entry as a function of time separated by entry location, solar wind entry is by no means a time-steady process and both entry mechanisms display quasiperiodic temporal variability. Flank entry is largely constant in magnitude as a function of time but exhibits smaller-scale temporal variability with a characteristic time scale of a few minutes. Cusp entry exhibits zeroth-order periodicity at a time scale of approximately 8 min, varying in magnitude from approximately equal to the flank entry rate up to 4 times the flank entry rate. The model predicted cusp entry rates are well in line with observational estimates (Hasegawa, 2012; Shi et al., 2013). We find that the periodicity observed in the cusp entry rate, approximately 8 min, known to be typical of flux-transfer events (Lockwood et al., 1990) corresponds to intermittent cusp reconnection events in our simulation. These time scales are potentially interesting in their relationship to observed type 2 pulsating cusp aurora (e.g., Sandholt et al., 1998); however, a thorough exploration of this is beyond the scope of this work.

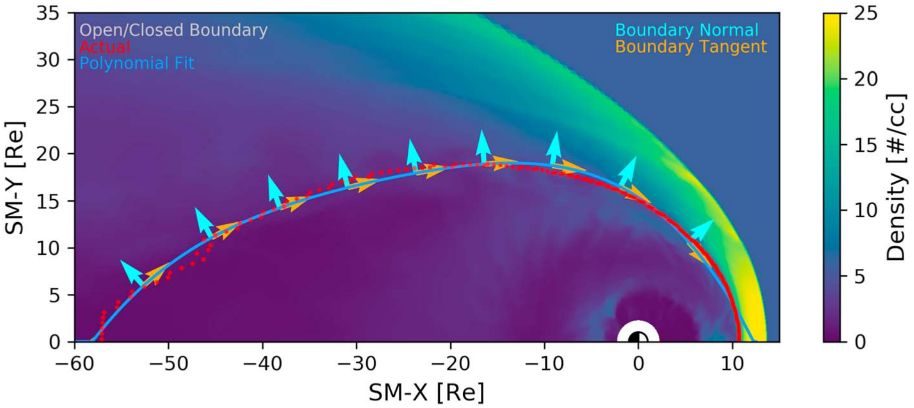

Figure 7. Fiducial magnetopause location as defined by the average location, as a function of longitude, of the equatorial open-closed boundary (dotted line) and smooth interpolant (solid line). The magnetopause boundary is used to construct a coordinate system defining directions tangential and normal (overlaid arrows) to the curve. Background shows time-averaged equatorial density for orientation.

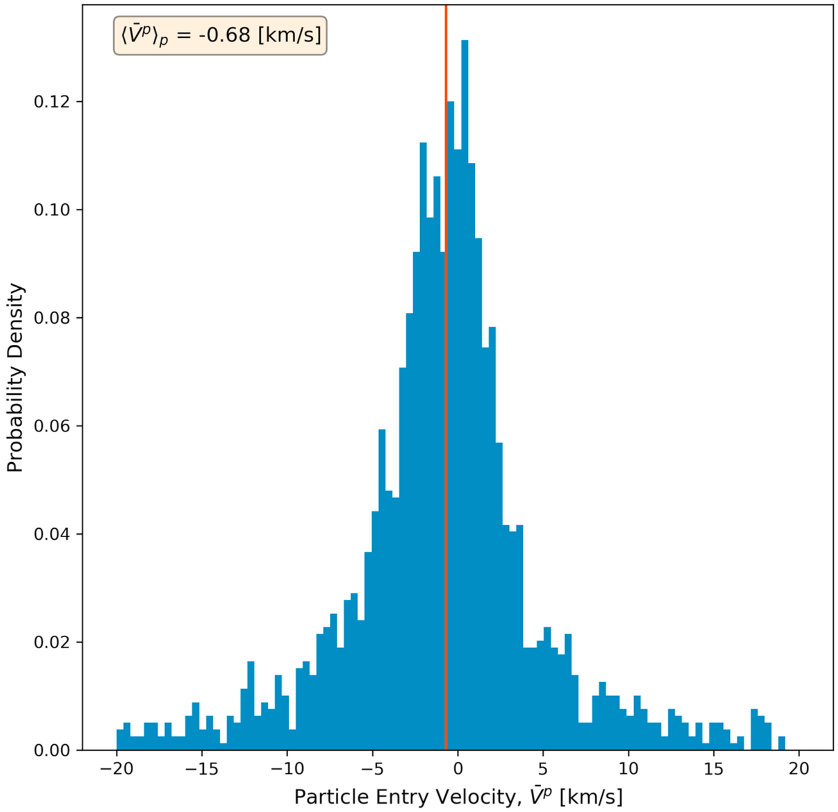

Figure 8. Entry velocity. Statistical distribution of entry velocities as defined by equation (A1) over all flank-entering test particles and the average taken over the test particle ensemble (red vertical line).

3.3. Analysis of Flank Entry

Figure 1 clearly illustrates that flank entry is localized in MLT, confined to a region approximately 4 hr (≈60°) on the dawn and dusk flanks downtail from the subsolar point, approximately $\phi_E \in [60°, 120°]$ or equivalently in MLT 1800 ± 0200 (dusk) and 0600 ± 0200 (dawn). To connect these entering test particles to KH vortices, we use here a simple metric of the strength of the boundary dynamics. Specifically, we use the root-mean-square (RMS) dawn-dusk velocity in the equatorial plane:

$$V_y^{\mathrm{RMS}}(r, \phi) = \sqrt{\frac{1}{T}\int_0^T V_y^2 \mathrm{d}t}, \tag{3}$$

where $T = 180$ min, the duration of the test particle simulation. The RMS V_y is shown in Figure 6 and is qualitatively similar to the more sophisticated spectral analysis of Merkin et al. (2013; e.g., their Figure 4) and also exhibits their observed double vortex structure. Overlaid on the RMS V_y in Figure 6 are solid lines representing the longitudinal domain of peak entry defined above.

Figure 6 illustrates that there is little low-latitude entry near the subsolar point and that the vast majority of low-latitude test particle entry, marked by the region between the green lines, occurs further downtail where the boundary becomes Kelvin-Helmholtz unstable. This is the converse of the result discussed by Sorathia et al. (2017) where it is found that the *egress* of magnetospheric plasma is inefficient within 0400 hr of magnetic noon, or $|\phi_E| \leq 60°$. These two results in tandem illustrate that boundary dynamics play an important role in regulating mass in the magnetosphere. More generally, this is an example of a mesoscale process (KHI) with global consequences for magnetospheric dynamics.

3.3.1. Transport Coefficients

Traditionally, the transport of mass through the magnetopause during northward IMF has been quantified using a diffusion coefficient calculated in two main ways: in terms of "blobby" transport velocities associated with reconnected large-scale magnetic islands and a typical system length scale (e.g., Nykyri & Otto, 2001) and via the mean square displacement of particles (e.g., Cowee et al., 2009; Nakamura et al., 2017). Despite

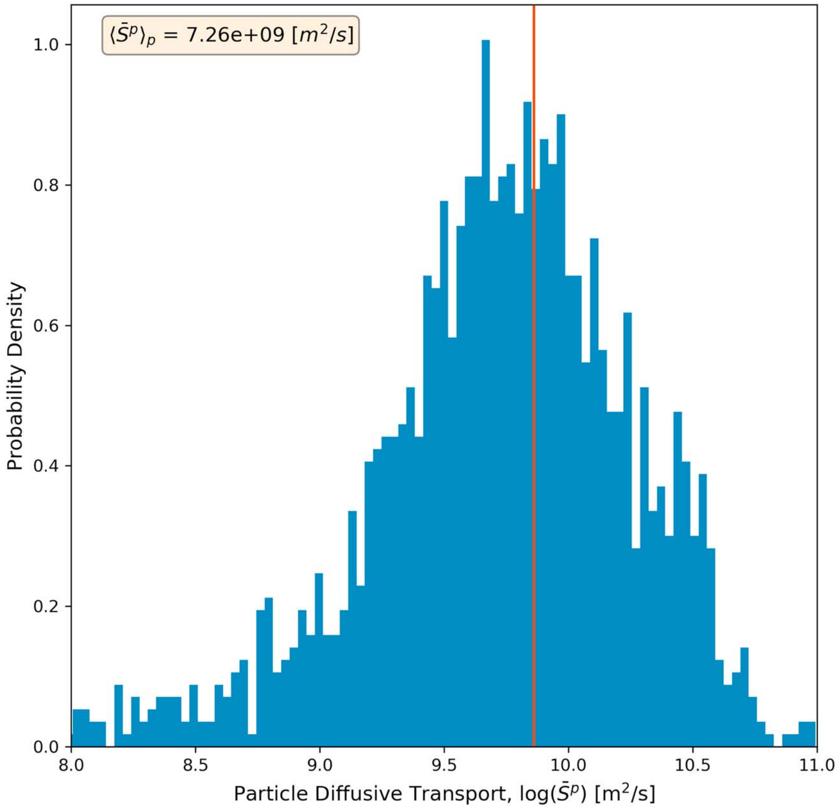

Figure 9. "Diffusion coefficient." Statistical distribution of diffusive transport as defined by equation (A2) over all flank-entering test particles and the average taken over the test particle ensemble (red vertical line).

the limitations of approximating transport as diffusive, there is an important benefit to be able to quantify transport efficacy with a single number. This provides some means to make comparisons between simulations utilizing different geometries and physical approximations. To this end, here we discuss transport coefficients calculated from our global simulation using test particle trajectories.

Estimation of the effective cross-boundary transport coefficients is fairly straightforward in the context of 2-D local simulations, but when moving to global 3-D simulations, caution and appropriate reinterpretation are necessary. The transport to be quantified, equatorial movement toward the central plasma sheet, happens on time scales (several to many hours) that are large when compared to particle bounce periods (minutes), the formation and dissipation of individual vortices with typical size several R_E ($\approx$ 20 min), and changes in the boundary normal direction over small scales ($\leq 1R_E$, tens of seconds). The boundary is sufficiently dynamic that it is difficult to separate particle motion across the boundary from boundary motion across the particle.

With the above caveats in mind, we find that the most natural connection between test particle behavior and plasma sheet filling is the motion of the equatorial crossing point in the direction normal to a fiducial magnetopause. We defer the full details of how we calculate transport coefficients to Appendix A and summarize them here. Despite the difficulty of appropriately treating spatial and temporal variability in the boundary geometry, the transport coefficients themselves exhibit little sensitivity, within a factor of order unity, to the exact details of the calculation.

Our analysis of transport utilizes an equatorial coordinate system, defining directions normal and tangent to a nominal magnetopause, taken to be a time-averaged location of the open-closed boundary (OCB). Figure 7 shows the data points resulting from the time average and the polynomial fit to those points we use to define the magnetopause. This curve then defines an orthogonal coordinate system in the tangential, $\hat{T}$, and normal, $\hat{N}$, directions, which is then extended throughout the equatorial plane. The basis vector is defined so that $\hat{N}$ always points away from the central plasma sheet. For each flank-entering test particle we can then define an entry velocity, $\bar{V}_p$ (equation (A1)), the net boundary normal displacement per time, and a

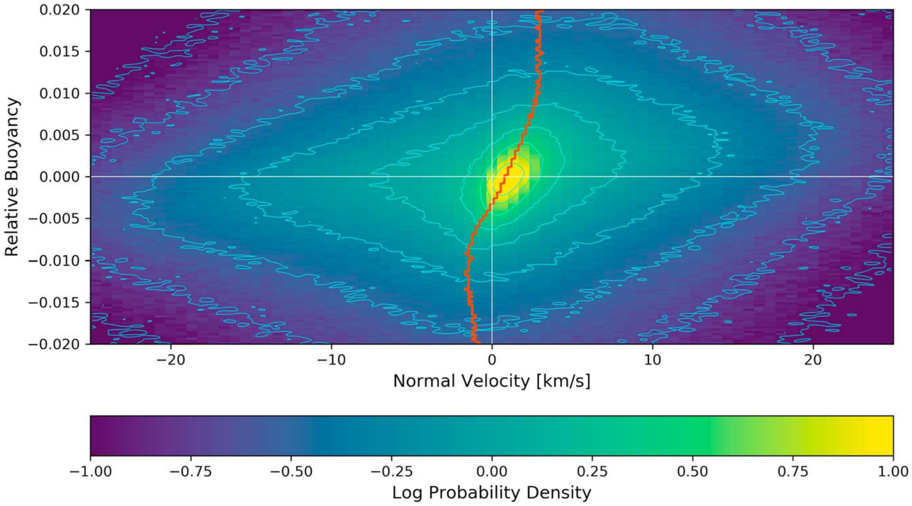

Figure 10. Role of interchange instability in flank transport. Correlation between relative buoyancy, defined by equation (5), and fluid velocity across nominal magnetopause boundary. Left (right) half represents movement toward (away) from the central plasma sheet. Top (bottom) half represent interchange unstable regions that will move away (toward) Earth. Overlaid are contours of constant probability density (cyan) and median boundary normal velocity for fixed relative buoyancy (red).

diffusion coefficient, $\bar{S_p}$ (equation (A2)), the mean square displacement of the particle in the frame moving at the particle's entry velocity. For the latter, the diffusion coefficient, we follow the notation of Cowee et al. (2010) and use S instead of D to avoid confusion with a classical diffusion coefficient.

The distribution of per-particle transport coefficients, defined in equations (A1) and A2, is shown in Figures 8 and 9. Representative transport coefficients, denoted as $\langle\cdot\rangle_p$, are calculated as an average over the per-particle transport coefficients. These average transport coefficients are marked by vertical lines and shown in the top left of Figures 8 and 9. The average entry velocity, $< \bar{V_p} >_p \approx -0.68$ km/s, although calculated differently, is very much in line with the results of Nykyri et al. (2017) that find plasma transport velocities ≤ 0.64 km/s using 2.5-D resistive MHD with multimode seeding of KH. Estimating an effective "diffusion coefficient" yields $< \bar{S_p} >_p \approx 7 \times 10^9$ m^2/s, which is in agreement with estimates calculated using a variety of different methods: 2.5-D resistive local MHD (e.g., Nykyri et al., 2017), 3-D resistive local MHD (Ma et al., 2017), hybrid (e.g., Cowee et al., 2009), and fully kinetic (e.g., Nakamura et al., 2013) simulations, as well as early analytic estimates of LLBL mass transport (e.g., Sonnerup, 1980). While treating transport as a diffusive process is sufficient for order of magnitude estimates, the mesoscale coherent motion of KH vortices and, as we show in the next section, interchange unstable flux tubes make a diffusive approximation inappropriate for more accurate analysis.

3.3.2. Interchange Instability in Flank Transport

Interchange instability, due to flux-tube entropy imbalance, has long been believed to play an important role in the earthward transport of magnetotail plasma (Chen & Wolf, 1993; Pontius & Wolf, 1990). Johnson and Wing (2009) discussed plasma sheet entropy during northward IMF and how it may vary depending on entry mechanism. Here we explore the connection between entropy and transport across the LLBL. To quantify the importance of interchange instability to a local region of interest, we can use the entropy function (i.e., Birn et al., 2009):

$$\mathcal{S}(R,\phi) = \int p(\vec{x})^{1/\gamma} \frac{\mathrm{d}s}{B(\vec{x})}, \tag{4}$$

where the integral is taken along flux tubes for each cell in the equatorial plane of our MHD simulation. The quantity $\mathcal{S}$ is related to but not exactly the thermodynamic entropy of a flux tube and also should not be confused with the diffusion coefficient, $\bar{S_p}$ defined in the previous section. Instability is governed by the deviation of the local entropy from the background (Rosenbluth & Longmire, 1957), which we quantify using

$$\delta\mathcal{S}(R,\phi,t) = \frac{\mathcal{S}(R,\phi,t) - \mathcal{S}_0(R,\phi,t)}{\mathcal{S}_0(R,\phi,t)}, \tag{5}$$

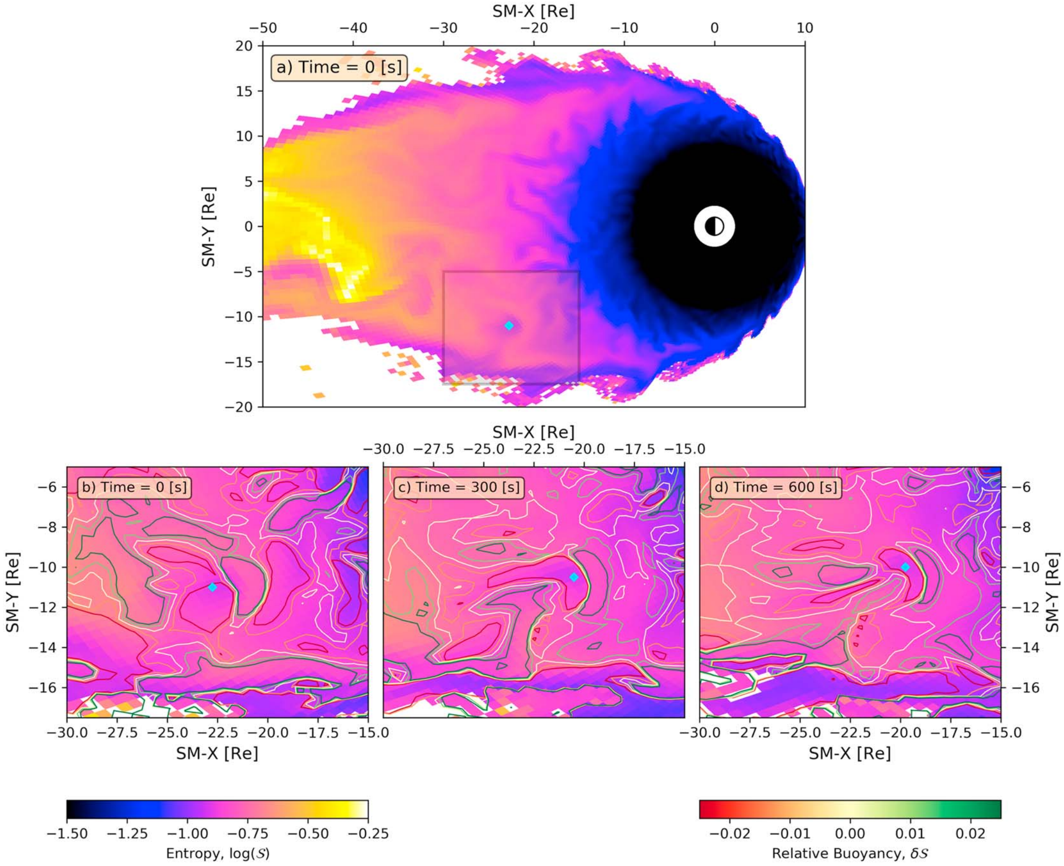

Figure 11. Example of flank transport via buoyancy. The top panel shows the equatorial distribution of entropy (equation (4)) at a chosen time along with a shaded rectangle to mark the region to be focused on in the bottom panels. The bottom panels show the time evolution of shaded region over 10 min and are overlain with contours of constant relative buoyancy (equation (5)), with red corresponding to low-entropy regions or bubbles. In all panels, diamond markers are manually placed on the moving bubble to guide the reader. SM = solar magnetic.

where $\mathcal{S}_0(R, \phi, t)$ is an average background entropy using a sliding window in time; that is,

$$\mathcal{S}_0(R, \phi, t) = \frac{1}{\delta t} \int_{t-\delta t/2}^{t+\delta t/2} \mathcal{S}(R, \phi, t), \tag{6}$$

where $\delta t = 10$ min. Equation (5) represents a "relative buoyancy," that is, the relative deviation of the local entropy from the background. Negative relative buoyancy corresponds to regions that will move toward lower $\mathcal{S}$, typically earthward, through interchange instability.

To improve our statistics and avoid the necessity of interpolation, we will look at the correlation of the MHD flow velocity, instead of test particle equatorial motion, with the relative buoyancy. At each spatial position and time that we calculate the relative buoyancy we can also calculate the boundary normal velocity by transforming the MHD (V_x, V_y) to the coordinate system illustrated in Figure 7. This correlation analysis is restricted to closed field regions near the nominal magnetopause boundary, $7.5R_E \leq |Y| \leq 25R_E$ and results in approximately 10^7 data points. Figure 10 shows the statistical distribution of relative buoyancy, $\delta\mathcal{S}$, and boundary normal flow velocity, V_N overlain with contours of constant density (cyan) and median normal velocity for fixed relative buoyancy (red).

The correlation between boundary normal flow velocity and relative buoyancy (equation (5)) is shown in Figure 10. The density contours illustrate the positive correlation between $\delta\mathcal{S}$ and V_N, with increasing buoyancy leading to median outward flow up to $V_N \approx 3$ km/s and decreasing buoyancy leading to inward flow, that is, toward the central plasma sheet, up to $V_N \approx -1.5$ km/s. The correlation is clearest for $|\delta\mathcal{S}| < 0.01$, regions that deviate by under 1% from the average background. Crudely, we find that $V_N \sim \delta\mathcal{S} \times 250$ (km/s)

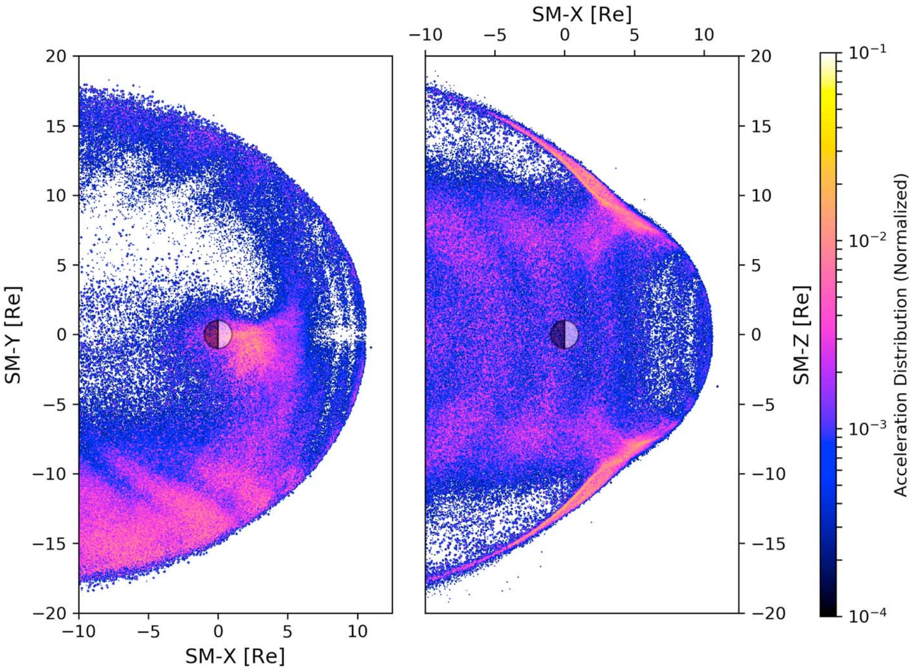

Figure 12. Distribution of total energy gained by cusp-entering population projected onto the X-Y (left) and X-Z (right) planes. SM = solar magnetic.

for $|\mathcal{S}| \leq 10^{-2}$. This transport behaves much like magnetotail transport, albeit in miniature. Typical entropy depletion and transport velocities of magnetotail transport are an order of magnitude larger.

An example of this manner of transport is highlighted in Figure 11, in which the time evolution of a bubble is shown over the course of 10 min. This example should not be taken to be typical; the transport velocity is $V \approx 20$ km/s and $\delta\mathcal{S} \approx 0.02$, which places it at the extreme range seen in Figure 10; it is merely chosen for illustrative purposes. The global entropy distribution exhibited (Figure 11a) is typical, however, and demonstrates the depleted regions that form on the leading edges of the KH vortices. Johnson and Wing (2009) consider changes in entropy across the magnetopause due to KH reconnection and estimate $\Delta\mathcal{S}/\mathcal{S}_0 \sim -\Delta B/B$, where the differences are taken between the magnetosphere and magnetosheath. We typically find weaker magnetic fields in the magnetosphere than in the magnetosheath, consistent with spacecraft observations (e.g., Taylor & Lavraud, 2008) and the expectation of flux pileup during northward IMF. Reconnection within KH vortices will then result in regions of magnetospheric flux tubes being replaced by magnetosheath counterparts with the effect of lowering the total entropy of the magnetospheric flux tube due to the reduced flux tube volume of the replacement.

Figures 11b–11d show the evolution of the highlighted region over time with contours of constant $\delta\mathcal{S}$ overlain. A marker is placed manually on the central region of the bubble for orientation. We see that the initial region of low entropy ($\delta\mathcal{S} < 0$) moves earthward with a corresponding high-entropy ($\delta\mathcal{S} > 0$) region in front, similar to what is seen of simulations of bubble injections during southward IMF (e.g., Yang et al., 2011). The motion of this bubble is not directly toward the central plasma sheet but also moves sunward. This behavior, and the speed of propagation, is consistent with the weakly sunward streaming population observed by Geotail described by Fujimoto et al. (1998).

3.4. Analysis of Cusp Entry

While we find that flank-entering plasma is dawn-dusk symmetric and undergoes minimal acceleration, the cusp-entering plasma is quite the opposite. Figure 3 illustrates that the majority of cusp-entering plasma moves along the dawnward flank and that cusp-entering plasma eventually observed near dusk is predominantly made up of energetic particles that cross the plasma sheet from dawn. In this section we show that the origin of this asymmetry and acceleration is due to the trajectories of ions through the cusp DMC as described by Nykyri et al. (2012).

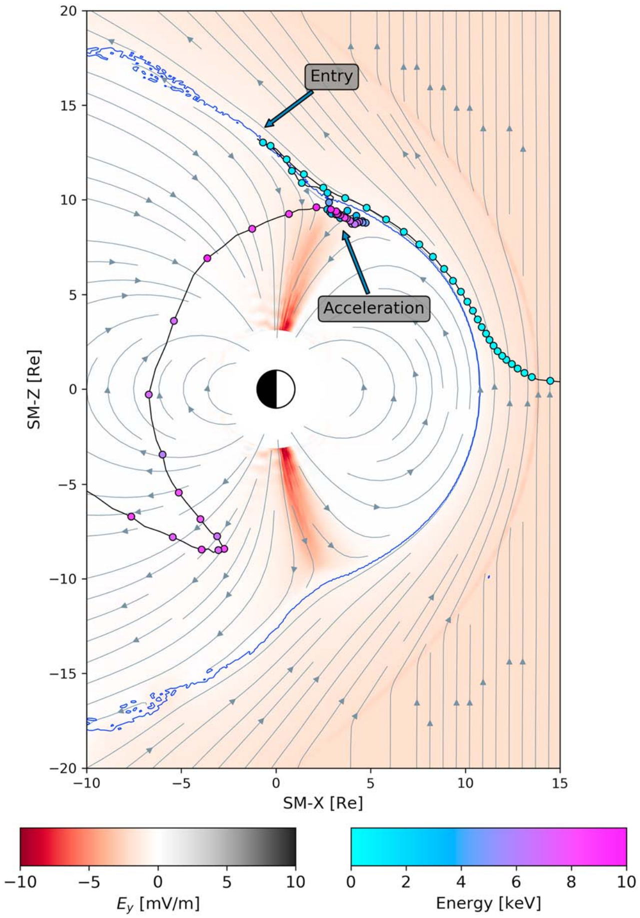

Figure 13. Example of acceleration of cusp-entering test particles. A fiducial trajectory, projected onto the X-Z plane, is shown colored by instantaneous particle energy (bottom right color bar). The dusk-dawn (SM-Y) component of the electric field is illustrated by the background color (bottom left color bar) with along with streamlines of meridional (B_x, B_z) magnetic field. The boundary between interplanetary magnetic field and open/closed field lines is shown as solid line (blue). Arrows mark regions where this test particle enters the magnetosphere and is accelerated in the cusp diamagnetic cavity. Note that the particle first moves antisunward to the point of entry and subsequently moves sunward to the region of acceleration. SM = solar magnetic.

It is shown by Figure 4 that the cusp-entering population is hotter than its flank-entering counterpart, which exhibits little change in energy as it transfers from the solar wind into the magnetosphere. As a first step toward understanding the source of the energy gained by cusp-entering particles we will identify the spatial region this acceleration occurs in. To this end we consider the spatial distribution of cusp-entering particle energization, which we denote $\mathcal{E}(x, y, z)$, defined to be the amount of energy gained (keV) by all cusp-entering test particles in the differential cube $[x, x + \Delta x] \times [y, y + \Delta y] \times [z, z + \Delta z]$ integrated in time over the duration of the test particle simulation. Under this definition the volume integral, $\int \mathcal{E} \mathrm{d}V$, is the total energy gained by all cusp-entering test particles. The energization distribution, in normalized units, is shown in Figure 12 in both the X-Y plane, integrated over Z (left), and in the X-Z plane, integrated over Y (right).

The geometry of the geomagnetic cusp is clearly highlighted by the distribution shown in Figure 12, which highlights a region several R_E sunward and dawnward of Earth and at high-latitude ($|\lambda| \geq 50°$ and altitude ($|Z| > 7R_E$). While this energization region is sunward of Earth, as shown in Figure 1 the vast majority of cusp-entering particles enter tailward, as would be expected from northward IMF cusp reconnection. The difference in entry and energization locations suggests the cause. It is known that during northward IMF a four-cell convection pattern often develops (Burke et al., 1979) in which there is a steady sunward flow across the polar caps. This flow can be seen as the $\vec{E} \times \vec{B}$ velocity, which we denote $V_{E\times B}$ associated with a dawnward electric field, as shown in Figure 13 for a fiducial snapshot in time. A simple estimate can demonstrate that the electric field is sufficiently strong to energize particles from ∼1 keV to the ∼25 keV that we observe in our simulation. Taking $\Delta K = qE\Delta y$, we get $\Delta K \approx 30$ keV using $E_y = -2.5$ mV/m and $\Delta y = 2R_E$, estimated from our simulation geometry. A typical trajectory of a cusp-entering particle is shown in Figure 13 overlaid on a snapshot of the electromagnetic fields at the time of its entry.

The dawn-dusk asymmetry of the cusp-entering particles is due to the combined effect of a dawnward electric field and westward ion drift orbits, duskward on the nightside and dawnward on the dayside, caused by the combined effect of gradient and curvature drifts, which we denote V_∇. It is only in the morning quadrant that the ion drift and electric field combine to produce energization. If we consider the particle velocity as a combination of the $\vec{E} \times \vec{B}$ velocity ($V_{E\times B}$) and energy-dependent drifts, curvature and gradient (V_∇), then the relative importance of the curvature and gradient drifts will scale with particle energy. For dayside particles, energization due to the dusk-dawn aligned electric field and drift velocity creates positive feedback as increasingly energetic particles become increasingly gradient and curvature drift dominated. While we find that some cusp-entering particles do immediately deflect duskward, this is rare and these particles, with typical solar wind energy, would easily blend in with the much larger dusk flank-entering population.

Also of note in Figure 12 is the secondary feature in the equatorial distribution of energization (left panel) on the dawnside flank beginning at 0800 MLT, precisely the KH-active region downtail of the subsolar point. Unlike flank-entering particles with typical energy $K \leq 1$ keV, cusp-entering particles reach the dawnside flank with typical energies $K \sim 10$ keV and will therefore exhibit trajectories in which the gradient and curvature drifts play a more important role. In the absence of a strong inductive electric field, a guiding center particle will energize according to $\Delta K = q\vec{V}_\nabla \cdot \vec{E}\Delta t$. The more energetic cusp-entering particles exhibit non-negligible V_∇, which can interact with the vortical flow structures and the resultant convective electric fields (e.g., Sorathia et al., 2017). This is in contrast to the colder, predominantly $\vec{E}\times\vec{B}$-drifting flank-entering population. This implies that the particles that end up in the prenoon flank shortly after entry, the majority of cusp-entering and half of the flank-entering, will subsequently evolve very differently due to their different entry mechanisms and resultant energization. We attribute the mesoscale structure in the secondary energization feature, the striping along the dawn flank seen in Figure 12, to quasiperiodic overlapping of the bursty cusp entry seen in Figure 5, and the alternating flow structures in the tailward propagating vortices on the dawn flank.

4. Discussion and Conclusions

We have described the methodology and results of a study of solar wind entry during northward IMF using global MHD and test particle simulations. We use high-resolution global MHD, LFM OCT resolution, to generate electromagnetic fields that can capture KH vortices (Merkin et al., 2013). The solar wind ions are modeled using a large ensemble of test particles, 50 million, injected over time upstream of the bow shock. This methodology allows us to capture nonfluid effects, such as drift physics, which we find to be important in the acceleration of cusp-entering particles while simultaneously resolving the global geometry of the magnetosphere and mesoscale boundary dynamics of the magnetopause. Additionally, this approach has allowed us to easily categorize and separately analyze particle trajectories based on their entry mechanism. The unique advantages of this modeling framework have enabled us to address enduring fundamental questions regarding the mechanism and characteristics of solar wind entry posed by observations.

Analyzing the collection of solar wind test particle trajectories that enter the magnetosphere during purely northward IMF has shown the following:

- Entering solar wind particles can be separated into two disjoint populations: flank-entering and cusp-entering particles (Figures 1 and 2), respectively providing (∼ 1/3) and (∼2/3) of the entering mass.
- Flank-entering particles enter the magnetosphere in a near-equatorial region downtail from the subsolar point and are relatively cold and dawn-dusk symmetric.
- Cusp-entering particles, those that enter the magnetosphere at high-latitude tailward of Earth, upon entry are predominantly deflected toward dawn.
- Both entry mechanisms exhibit quasiperiodic variability (Figure 5), 2–3 min for flank entry and ∼8 min for cusp entry.

We find that the two entry populations, flank and cusp entering, differ in far more than just their point of entry. Individual analysis of each population shows that they are subject to different transport and energization mechanisms during and subsequent to their magnetospheric entry. Our analysis of flank-entering particles shows the following:

- The effective diffusive transport rate for flank-entering particles, $\approx 7 \times 10^9$ m^2/s, is similar to localized resistive MHD simulations, hybrid, and kinetic simulations.
- Correlation of magnetopause boundary normal velocity to the total flux-tube entropy (Figure 10) shows that interchange instability plays a role in the transport of plasma toward the central plasma sheet.
- The typical depleted entropy regions seen on both dawn and dusk flanks (Figure 11) can be interpreted as the result of reconnection within KH vortices that replaces regions of magnetospheric flux tubes with lower-volume magnetosheath counterparts.

Separately analyzing cusp-entering particles has shown that

- Particles that enter through the cusp often become energized due to the alignment of a dawnward electric field, due to four-cell convection typical of northward IMF, and the westward ion drift (Figure 13).
- Unlike flank-entering particles that are largely passively advected with the bulk flow, cusp-entering particles exhibit drift dynamics due to their energization during entry.
- Cusp-entering particles are predominantly deflected toward dawn where the most energetic are able to cross the plasma sheet due to their westward drift.
- Cusp-entering particles, due to their higher energies when they encounter the dawn flank, can further energize due to the alignment of energy-dependent drift (gradient and curvature) with the alternating convective electric fields of KH vortices.

Finally, considering the combined effect of both entering solar wind populations shows that the dawn-dusk asymmetry that is observed in nature emerges from our idealized and symmetric simulation (Figure 4). Specifically, we find that

- The dawn ion population is composed of cold flank-entering ions and a smooth range of energized cusp-entering particles.
- The dusk ion population is composed of the same cold flank-entering ions and a higher-energy subset of the cusp-entering particles, namely, those energetic enough to cross the central plasma sheet from dawn to dusk.
- The dawn ion population is hotter and more numerous than the dusk population and exhibits a smooth broad peak in energy distribution.
- The dusk ion population exhibits a two-component thermodynamic structure due to the cold flank-entering ions and the high-energy subset of the cusp-entering ions.
- The entry of solar wind through the geomagnetic cusp during northward IMF, absent any extrinsic asymmetry, creates an intrinsic source of dawn-dusk asymmetry in mass and temperature.

Although based on a single simulation with idealized symmetry, this work is a step toward a deeper understanding of the processes that regulate mass in the terrestrial plasma sheet. Further study of the solar wind parameter space and more realistic solar wind conditions is necessary as is the continued use of models that incorporate physics beyond ideal MHD, including resistive MHD, hybrid, and kinetic. It is possible that other, extrinsic factors during realistic solar wind conditions will add asymmetries to the solar wind entry beyond that we describe here. In addition, ideal MHD is unable to address potentially important kinetic effects, for example, KAWs. With these points in mind, this work demonstrates that, given sufficient resolving power, modern global MHD models of the magnetosphere can capture KH transport that has previously been the exclusive realm of more localized treatments. Going forward, we expect that global modeling will play a greater role in the study of transport across the terrestrial and other planetary magnetospheric boundaries.

These results taken together with Sorathia et al. (2017), who discuss the role of boundary dynamics in the loss of magnetospheric plasma, paint a picture of the magnetopause very different than its cartoon interpretation as a static boundary that is traversed due to individual particle dynamics. Instead, we find the magnetopause to be an active participant in regulating the transfer of mass and energy between the magnetosphere and solar wind. Boundary dynamics, in the form KH vortices, facilitates the loss of magnetospheric plasma into the magnetosheath and through intravortex reconnection, creating low-entropy flux tubes, the entry and transport of magnetosheath plasma toward the central plasma sheet. These effects are not merely next-order corrections, but rather, they are a core physical mechanism of particle transport across the magnetopause. Capturing these mesoscale interactions is a necessary condition for any global description of the magnetosphere.

Appendix A: Calculation of Transport Coefficients

Here we describe the exact manner in which we use a collection of 3-D test particle trajectories within global MHD fields to calculate the transport coefficients, entry velocity, and diffusion, that we discuss in section 3.3.1. We proceed in three steps: define an appropriate coordinate system in the equatorial plane to separate transport across the magnetopause boundary from transport transverse to it; for each particle calculate an entry velocity, $\bar{V}_p$ the boundary normal displacement per time, using that particle's equatorial crossings; and finally calculate a diffusion coefficient for each particle, $\bar{S}_p$ the mean square displacement in the frame moving at the particles entry velocity. Finally, averaging the transport coefficients over the particle ensemble gives us fiducial global values of each.

Our goal is to quantify transport across the magnetopause over time scales of several hours, and we begin by finding a fiducial equatorial magnetopause boundary. We define the nominal magnetopause as the time-averaged location, taken over the simulation duration and as a function of longitude, of the OCB. These data points are shown in Figure 7 along with a polynomial fit to the curve, which we will henceforth treat as the OCB. The OCB can be used to define an orthogonal coordinate system on the curve in the tangential, $\hat{T}$, and normal, $\hat{N}$, directions. Figure 7 shows the result for the postnoon sector. The basis vectors are defined so that $\hat{T}$ is always sunward and $\hat{N}$ always points away from the central plasma sheet. Next we extend the coordinate system to the entire postnoon sector, with the prenoon sector coordinate system following by symmetry. The basis vectors for an arbitrary point (x, y) are defined to equal the basis vectors at the point $(x_{\text{MP}}, y_{\text{MP}})$, the point on the magnetopause boundary closest to (x, y).

In this analysis, we use $\mathcal{P}$ to refer to the collection of solar wind test particles that enter the magnetosphere through the flank, meaning that particles in $\mathcal{P}$ transition from IMF to terrestrial, open or closed, magnetic field lines at low latitude ($|\lambda_E| \leq 25°$) and for some period of time, which we take to be 15 min, remain on closed magnetic field lines. From this collection of particles, we consider only equatorial crossings that occur after entry, when the particle transitions from IMF to either open or closed field lines, and while on either open or closed field lines. We define $(X_N, X_T, T_{EQ})^{i,p}$ as the location, in the boundary coordinate system, and time of the ith equatorial crossing of particle $p \in \mathcal{P}$. In what follows we will disregard the tangential direction and treat the transport as one-dimensional along the normal direction. Using these definitions, $\Delta X_N < 0$ corresponds to entry.

The entry velocity for a particle p is given by

$$\bar{V}_p = \frac{X_N^{n,p} - X_N^{1,p}}{T_{EQ}^{n,p} - T_{EQ}^{1,p}}, \tag{A1}$$

where $i = 1$ and $i = n$ are the first and last equatorial crossings recorded for particle p that satisfy the criteria above.

The particle diffusive transport, the mean square displacement in the frame moving at the entry velocity, is then defined as

$$\bar{S}_p = \frac{1}{2N_D \Delta T^p} \sum_i \left[(X_N^{i+1,p} - X_N^{i,p}) - \bar{V}_p (T_{EQ}^{i+1,p} - T_{EQ}^{i,p}) \right]^2, \tag{A2}$$

where $\Delta T^p = T_{EQ}^{n,p} - T_{EQ}^{1,p}$, the total time the particle spends in the magnetosphere, and we use $N_D = 2$, corresponding to transport in the plane. Following Cowee et al. (2010), we use the notation S instead of D to avoid confusion with a classical diffusion coefficient.

Acknowledgments
This work was supported by NASA Grants NNX14AH77G, NNX16AG73G, 80NSSC17K0679, and 80NSSC18K1381 and the Van Allen Probes contract NNN06AA01C. S. W. acknowledges support from NASA Grants NNX15AJ01G and NNX16AQ87G. K. N. acknowledges support from NASA Grants NNX17AI50G and NNX16AF89G. We would like to acknowledge the use of computational resources (doi:10.5065/D6RX99HX) at the NCAR-Wyoming Supercomputing Center provided by the National Science Foundation and the State of Wyoming and supported by NCAR's Computational and Information Systems Laboratory. A large sample of simulation data are provided in supporting information Data Set S1.

References

Adamson, E., Nykyri, K., & Otto, A. (2016). The Kelvin–Helmholtz instability under Parker-Spiral interplanetary magnetic field conditions at the magnetospheric flanks. *Advances in Space Research*, *58*(2), 218–230.

Allen, R. C., Livi, S. A., Vines, S. K., Goldstein, J., Cohen, I., Fuselier, S. A., et al. (2017). Storm time empirical model of O^+ and O^{6+} distributions in the magnetosphere. *Journal of Geophysical Research: Space Physics*, *122*, 8353–8374. https://doi.org/10.1002/2017JA024245

Birn, J., Hesse, M., Schindler, K., & Zaharia, S. (2009). Role of entropy in magnetotail dynamics. *Journal of Geophysical Research*, *114*, A00D03. https://doi.org/10.1029/2008JA014015

Borovsky, J. E., Thomsen, M. F., & Elphic, R. C. (1998). The driving of the plasma sheet by the solar wind. *Journal of Geophysical Research*, *103*(A), 17,617–17,640.

Burke, W. J., Kelley, M. C., Sagalyn, R. C., Smiddy, M., & Lai, S. T. (1979). Polar cap electric field structures with a northward interplanetary magnetic field. *Geophysical Research Letters*, *6*(1), 21–24.

Chen, C. X., & Wolf, R. A. (1993). Interpretation of high-speed flows in the plasma sheet. *Journal of Geophysical Research*, *98*(A12), 21,409–21,419.

Cowee, M. M., Winske, D., & Gary, S. P. (2009). Two-dimensional hybrid simulations of superdiffusion at the magnetopause driven by Kelvin-Helmholtz instability. *Journal of Geophysical Research*, *114*, A10209. https://doi.org/10.1029/2009JA014222

Cowee, M. M., Winske, D., & Gary, S. P. (2010). Hybrid simulations of plasma transport by Kelvin-Helmholtz instability at the magnetopause: Density variations and magnetic shear. *Journal of Geophysical Research*, *115*, A06214. https://doi.org/10.1029/2009JA015011

Fedder, J. A., & Lyon, J. G. (1995). The Earth's magnetosphere is 165 R(sub E) long: Self-consistent currents, convection, magnetospheric structure, and processes for northward interplanetary magnetic field. *Journal of Geophysical Research*, *100*(A3), 3623–3635.

Fujimoto, M., Terasawa, T., Mukai, T., Saito, Y., Yamamoto, T., & Kokubun, S. (1998). Plasma entry from the flanks of the near-Earth magnetotail: Geotail observations. *Journal of Geophysical Research*, *103*(A3), 4391–4408.

Guo, X. C., Wang, C., & Hu, Y. Q. (2010). Global MHD simulation of the Kelvin-Helmholtz instability at the magnetopause for northward interplanetary magnetic field. *Journal of Geophysical Research*, *115*, A10218. https://doi.org/10.1029/2009JA015193

Hasegawa, H. (2012). Structure and dynamics of the magnetopause and its boundary layers. *Monographs on Environment*, *1*(2), 71–119.

Hasegawa, H., Fujimoto, M., Maezawa, K., Saito, Y., & Mukai, T. (2003). Geotail observations of the dayside outer boundary region interplanetary magnetic field control and dawn-dusk asymmetry. *Journal of Geophysical Research*, *108*(A4), 1065. https://doi.org/10.1029/2002JA009667

Hasegawa, H., Fujimoto, M., Saito, Y., & Mukai, T. (2004). Dense and stagnant ions in the low-latitude boundary region under northward interplanetary magnetic field. *Geophysical Research Letters*, *31*, L06802. https://doi.org/10.1029/2003GL019120

Hesse, M., Schindler, K., Birn, J., & Kuznetsova, M. (1999). The diffusion region in collisionless magnetic reconnection. *Physics of Plasmas*, *6*(5), 1781–1795.

Hockney, R. W., & Eastwood, J. W. (1981). Computer simulation using particles. Computer Simulation Using Particles, New York: McGraw-Hill, 1981, Provided by the SAO/NASA Astrophysics Data System, http://adsabs.harvard.edu/abs/1981csup.book.....H

Johnson, J. R., & Wing, S. (2009). Northward interplanetary magnetic field plasma sheet entropies. *Journal of Geophysical Research*, *114*, A00D08. https://doi.org/10.1029/2008JA014017

Johnson, J. R., Wing, S., & Delamere, P. A. (2014). Kelvin Helmholtz instability in planetary magnetospheres. *Space Science Reviews*, *184*(1-4), 1–31.

Lehe, R., Parrish, I. J., & Quataert, E. (2009). The heating of test particles in numerical simulations of ALfvénic turbulence. *The Astrophysical Journal*, *707*(1), 404–419.

Li, W., Raeder, J., Thomsen, M. F., & Lavraud, B. (2008). Solar wind plasma entry into the magnetosphere under northward IMF conditions. *Journal of Geophysical Research*, *113*, A04204. https://doi.org/10.1029/2007JA012604

Lockwood, M., Cowley, S. W. H., & Sandholt, P. E. (1990). Transient reconnection: Search for ionospheric signatures. *Eos, Transactions American Geophysical Union*, *71*(20), 709–720.

Lyon, J. G., Fedder, J. A., & Mobarry, C. M. (2004). The Lyon–Fedder–Mobarry (LFM) global MHD magnetospheric simulation code. *Journal of Atmospheric and Solar-Terrestrial Physics*, *66*(15-16), 1333–1350.

Ma, X., Delamere, P., Otto, A., & Burkholder, B. (2017). Plasma transport driven by the three-dimensional Kelvin-Helmholtz instability. *Journal of Geophysical Research: Space Physics*, *122*, 10,382–10,395. https://doi.org/10.1002/2017JA024394

Merkin, V. G., & Lyon, J. G. (2010). Effects of the low-latitude ionospheric boundary condition on the global magnetosphere. *Journal of Geophysical Research*, *115*, A10202. https://doi.org/10.1029/2010JA015461

Merkin, V. G., Lyon, J. G., & Claudepierre, S. G. (2013). Kelvin-Helmholtz instability of the magnetospheric boundary in a three-dimensional global MHD simulation during northward IMF conditions. *Journal of Geophysical Research: Space Physics*, *118*, 5478–5496. https://doi.org/10.1002/jgra.50520

Miura, A. (1984). Anomalous transport by magnetohydrodynamic Kelvin-Helmholtz instabilities in the solar wind-magnetosphere interaction. *Journal of Geophysical Research*, *89*(A2), 801–818.

Miura, A. (1987). Simulation of Kelvin-Helmholtz instability at the magnetospheric boundary. *Journal of Geophysical Research*, *92*(A4), 3195–3206. https://doi.org/10.1029/JA092iA04p03195

Moore, T. W., Nykyri, K., & Dimmock, A. P. (2016). Cross-scale energy transport in space plasmas. *Nature Physics*, *12*, 1164–1169. https://doi.org/10.1038/nphys3869

Nakamura, T. K. M., Daughton, W., Karimabadi, H., & Eriksson, S. (2013). Three-dimensional dynamics of vortex-induced reconnection and comparison with THEMIS observations. *Journal of Geophysical Research: Space Physics*, *118*, 5742–5757. https://doi.org/10.1002/jgra.50547

Nakamura, T. K. M., Hasegawa, H., Daughton, W., Eriksson, S., Li, W. Y., & Nakamura, R. (2017). Turbulent mass transfer caused by vortex induced reconnection in collisionless magnetospheric plasmas. *Nature Communications*, *8*(1), 1582.

Niehof, J. T., Fritz, T. A., Friedel, R. H. W., & Chen, J. (2010). Size and location of cusp diamagnetic cavities observed by Polar. *Journal of Geophysical Research*, *115*, A07201. https://doi.org/10.1029/2009JA014827

Nishino, M. N., Fujimoto, M., Terasawa, T., Ueno, G., Maezawa, K., Mukai, T., & Saito, Y. (2007). Geotail observations of temperature anisotropy of the two-component protons in the dusk plasma sheet. *Annales Geophysicae*, *25*(3), 769–777.

Nishino, M. N., Fujimoto, M., Ueno, G., Maezawa, K., Mukai, T., & Saito, Y. (2007). Geotail observations of two-component protons in the midnight plasma sheet. *Annales Geophysicae*, *25*(1), 2229–2245.

Nykyri, K. (2013). Impact of MHD shock physics on magnetosheath asymmetry and Kelvin-Helmholtz instability. *Journal of Geophysical Research: Space Physics*, *118*, 5068–5081. https://doi.org/10.1002/jgra.50499

Nykyri, K., Ma, X., Dimmock, A., Foullon, C., Otto, A., & Osmane, A. (2017). Influence of velocity fluctuations on the Kelvin-Helmholtz instability and its associated mass transport. *Journal of Geophysical Research: Space Physics*, *122*, 9489–9512. https://doi.org/10.1002/2017JA024374

Nykyri, K., & Otto, A. (2001). Plasma transport at the magnetospheric boundary due to reconnection in Kelvin-Helmholtz vortices. *Geophysical Research Letters*, *28*(1), 3565–3568.

Nykyri, K., Otto, A., Adamson, E., Kronberg, E., & Daly, P. (2012). On the origin of high-energy particles in the cusp diamagnetic cavity. *Journal of Atmospheric and Solar-Terrestrial Physics*, *87*, 70–81.

Otto, A., & Fairfield, D. H. (2000). Kelvin-Helmholtz instability at the magnetotail boundary: MHD simulation and comparison with Geotail observations. *Journal of Geophysical Research*, *105*(A), 21,175–21,190.

Otto, A., & Nykyri, K. (2003). Kelvin-Helmholtz instability and magnetic reconnection: Mass transport at the LLBL. *Earth's Low-Latitude Boundary Layer*, *133*, 53–62.

Peroomian, V., & El Alaoui, M. (2008). The storm-time access of solar wind ions to the nightside ring current and plasma sheet. *Journal of Geophysical Research*, *113*, A06215. https://doi.org/10.1029/2007JA012872

Peroomian, V., El Alaoui, M., & Brandt, P. C. (2011). The ion population of the magnetotail during the 17 April 2002 magnetic storm: Large-scale kinetic simulations and IMAGE/HENA observations. *Journal of Geophysical Research*, *116*, A05214. https://doi.org/10.1029/2010JA016253

Pontius, D. H. Jr, & Wolf, R. A. (1990). Transient flux tubes in the terrestrial magnetosphere. *Geophysical Research Letters*, *17*(1), 49–52.

Raeder, J., Berchem, J., & Ashour-Abdalla, M. (1998). The Geospace Environment Modeling grand challenge: Results from a global geospace circulation model. *Journal of Geophysical Research*, *103*(A), 14,787–14,798.

Raeder, J., Walker, R. J., & Ashour-Abdalla, M. (1995). The structure of the distant geomagnetic tail during long periods of northward IMF. *Geophysical Research Letters*, *22*(4), 349–352.

Rosenbluth, M. N., & Longmire, C. L. (1957). Stability of plasmas confined by magnetic fields. *Annals of Physics*, *1*(2), 120–140.

Sandholt, P. E., Farrugia, C. J., & Cowley, S. W. H. (1998). Pulsating cusp aurora for northward interplanetary magnetic field. *Journal of Geophysical Research*, *103*(A11), 26,507–26,520.

Shi, Q. Q., Zong, Q. G., Fu, S. Y., Dunlop, M. W., Pu, Z. Y., Parks, G. K., et al. (2013). Solar wind entry into the high-latitude terrestrial magnetosphere during geomagnetically quiet times. *Nature Communications*, *4*(1), 1466.

Sonnerup, B. U. O. (1980). Theory of the low-latitude boundary layer. *Journal of Geophysical Research*, *85*(A5), 2017–2026.

Sorathia, K., Merkin, V. G., Ukhorskiy, A. Y., Mauk, B. H., & Sibeck, D. G. (2017). Energetic particle loss through the magnetopause: A combined global MHD and test-particle study. *Journal of Geophysical Research: Space Physics*, *122*, 9329–9343. https://doi.org/10.1002/2017JA024268

Sorathia, K., Ukhorskiy, A. Y., Merkin, V. G., Fennell, J. F., & Claudepierre, S. G. (2018). Modeling the depletion and recovery of the outer radiation belt during a geomagnetic storm: Combined MHD and test particle simulations. *Journal of Geophysical Research: Space Physics*, *123*, 5590–5609. https://doi.org/10.1029/2018JA025506

Taylor, M. G. G. T., & Lavraud, B. (2008). Observation of three distinct ion populations at the Kelvin-Helmholtz-unstable magnetopause. *Annales Geophysicae*, *26*(6), 1559–1566.

Wang, C.-P., Lyons, L. R., Nagai, T., Weygand, J. M., & McEntire, R. W. (2007). Sources, transport, and distributions of plasma sheet ions and electrons and dependences on interplanetary parameters under northward interplanetary magnetic field. *Journal of Geophysical Research*, *112*, A10224. https://doi.org/10.1029/2007JA012522

Welling, D. T., & Ridley, A. J. (2010). Exploring sources of magnetospheric plasma using multispecies MHD. *Journal of Geophysical Research*, *115*, A04201. https://doi.org/10.1029/2009JA014596

Wiltberger, M., Merkin, V., Lyon, J. G., & Ohtani, S. (2015). High-resolution global magnetohydrodynamic simulation of bursty bulk flows. *Journal of Geophysical Research: Space Physics*, *120*, 4555–4566. https://doi.org/10.1002/2015JA021080

Wing, S., Johnson, J. R., Chaston, C. C., Echim, M., Escoubet, C. P., Lavraud, B., et al. (2014). Review of solar wind entry into and transport within the plasma sheet. *Space Science Reviews*, *184*(1-4), 33–86.

Wing, S., Johnson, J. R., & Fujimoto, M. (2006). Timescale for the formation of the cold-dense plasma sheet: A case study. *Geophysical Research Letters*, *33*, L23106. https://doi.org/10.1029/2006GL027110

Wing, S., Johnson, J. R., Newell, P. T., & Meng, C. I. (2005). Dawn-dusk asymmetries, ion spectra, and sources in the northward interplanetary magnetic field plasma sheet. *Journal of Geophysical Research*, *110*, A08205. https://doi.org/10.1029/2005JA011086

Yang, J., Toffoletto, F. R., Wolf, R. A., & Sazykin, S. (2011). RCM-E simulation of ion acceleration during an idealized plasma sheet bubble injection. *Journal of Geophysical Research*, *116*, A05207. https://doi.org/10.1029/2010JA016346

Zhang, B., Lotko, W., Brambles, O., Damiano, P., Wiltberger, M., & Lyon, J. (2012). Magnetotail origins of auroral Alfvénic power. *Journal of Geophysical Research*, *117*, A09205. https://doi.org/10.1029/2012JA017680